



**HAL**  
open science

# Hydration Properties and Interlayer Organization of Water and Ions in Synthetic Na-Smectite with Tetrahedral Layer Charge. Part 1. Results from X-ray Diffraction Profile Modeling

Eric Ferrage, Bruno Lanson, Laurent J. Michot, Jean-Louis Robert

► **To cite this version:**

Eric Ferrage, Bruno Lanson, Laurent J. Michot, Jean-Louis Robert. Hydration Properties and Interlayer Organization of Water and Ions in Synthetic Na-Smectite with Tetrahedral Layer Charge. Part 1. Results from X-ray Diffraction Profile Modeling. *Journal of Physical Chemistry C*, 2010, 114, pp.4515-4526. 10.1021/jp909860p . insu-00545005

**HAL Id: insu-00545005**

**<https://insu.hal.science/insu-00545005v1>**

Submitted on 9 Nov 2011

**HAL** is a multi-disciplinary open access archive for the deposit and dissemination of scientific research documents, whether they are published or not. The documents may come from teaching and research institutions in France or abroad, or from public or private research centers.

L'archive ouverte pluridisciplinaire **HAL**, est destinée au dépôt et à la diffusion de documents scientifiques de niveau recherche, publiés ou non, émanant des établissements d'enseignement et de recherche français ou étrangers, des laboratoires publics ou privés.

# Hydration Properties and Interlayer Organization of Water and Ions in Synthetic Na-Smectite with Tetrahedral Layer Charge. Part 1. Results from X-ray Diffraction Profile Modeling

Eric Ferrage,<sup>\*,†</sup> Bruno Lanson,<sup>‡</sup> Laurent J. Michot,<sup>§</sup> and Jean-Louis Robert<sup>||</sup>

Laboratoire Hydrogéologie, Argiles, Sols et Altérations, UMR6269-CNRS, Université de Poitiers, 40 avenue du Recteur Pineau, 86022 Poitiers Cedex, France, Mineralogy & Environments, LGCA - Maison des Géosciences, CNRS - Université Joseph Fourier, BP53, 38041 Grenoble cedex 9, France, Laboratoire Environnement et Minéralurgie, Nancy University, CNRS-INPL UMR 7569 BP40 54501, Vandoeuvre Cedex, France, and IMPMC Campus Boucicaut, 140 rue de Lourmel, F-75015 Paris, France

Received: October 14, 2009; Revised Manuscript Received: January 7, 2010

The dehydration of two Na-saturated synthetic saponites with contrasting layer charge was studied by modeling the X-ray diffraction (XRD) patterns recorded along a water vapor desorption isotherm. The interlayer configurations used to reproduce the XRD data over a large angular range include Na<sup>+</sup> cations located in the interlayer midplane and H<sub>2</sub>O molecules normally distributed about one or two main positions for mono- and bihydrated layers, respectively. Although strongly reduced in comparison to natural smectites, hydration heterogeneity was systematically observed for these synthetic saponites, especially along the transition between two hydration states. Using improved models for the description of the interlayer organization, the influence of layer charge on the structure of interlayer water can be precisely assessed. In addition, the comparison with water contents obtained from water vapor gravimetry experiments allows discriminating the relative contributions of H<sub>2</sub>O molecules from 1W and 2W interlayers (crystalline water) and from the pore space network.

## Introduction and Background Information

Smectites are clay minerals ubiquitous in surface environments, both terrestrial and marine, where they often represent one of the main mineral components. Their structure involves colloidal size (<2 μm) negatively charged layers constituted with two tetrahedral sheets sandwiching an octahedral one. The main valence of the cations of the octahedral sheet defines the trioctahedral (divalent cations) or dioctahedral (trivalent cation) classification among the smectite mineral group. The charge deficit resulting from cationic substitutions in either the tetrahedral or octahedral sheet is compensated for by exchangeable cations located in the interlayer space. The moderate charge of the layers (between −0.1 and −0.2 C/m<sup>2</sup>) allows water molecules to penetrate the interlayer space and hydrate the interlayer cations, which results in a swelling of the crystal structure. As a consequence, smectite minerals exert a key influence on the hydration capacity of soils and on the fate of contaminants and plant nutrients therein.<sup>1</sup> Similarly, smectite dehydration in sedimentary rocks releases large amounts of fluids possibly giving rise to hydrothermalism.<sup>2–4</sup> Smectites are also observed in plate-boundary faults, where their rheological behavior and its evolution upon dehydration likely contributes to slipping processes.<sup>5–9</sup> Understanding the organization of hydrated interlayer species in smectite minerals is thus of prime importance for assessing the physical and chemical reactivity of numerous environments where those minerals are present.

Pioneering X-ray diffraction (XRD) studies of smectite hydration analyzed the position of 00*l* basal reflections as a function of relative humidity, and revealed a stepwise expansion, the different steps corresponding to the intercalation of 0, 1, 2, or 3 planes of H<sub>2</sub>O molecules in the interlayer.<sup>10–14</sup> Different layer types were thus defined for smectite: dehydrated (0W,  $d_{001} = 9.7–10.2$  Å), monohydrated (1W,  $d_{001} = 11.6–12.9$  Å), bihydrated (2W,  $d_{001} = 14.9–15.7$  Å), and trihydrated (3W,  $d_{001} = 18–19$  Å) layers, the latter being less common. However, it was soon recognized that different hydration states/layer types usually coexist even under controlled conditions due to structural heterogeneities affecting the layer charge distribution (from one interlayer to the other or within a given interlayer) and/or location.<sup>15–19</sup> Such a coexistence is for instance revealed by the irrationality of the 00*l* reflection series and by peak profile asymmetry at the transition between two hydration states.<sup>19,20</sup> XRD profile modeling procedures were thus developed to quantify hydration heterogeneity of smectite as a function of relative humidity.<sup>21–24</sup> By fitting positions and profiles of the 00*l* reflections over a large angular range, the relative proportions of the different layer types can be determined together with the thickness and water content of the different layer types.<sup>20,25,26</sup> These studies showed systematic hydration heterogeneity whatever the interlayer cation, relative humidity (RH), amount, and location of layer charge and temperature.

Taking smectite hydration heterogeneity into account is thus an essential prerequisite for investigating the organization of interlayer water in detail.<sup>27</sup> Despite XRD low sensitivity to low-Z elements (and especially hydrogen atoms), some attempts have been made to assess such organization on the basis of modeling of 00*l* basal reflections. For instance the interlayer configuration proposed by Moore and Reynolds for 2W layers<sup>28</sup> was replaced by an alternative configuration with a unique plane of H<sub>2</sub>O

\* To whom correspondence should be addressed. Phone: +33 (0)5 49 36 64 09. E-mail: eric.ferrage@univ-poitiers.fr.

<sup>†</sup> Université de Poitiers.

<sup>‡</sup> Université Joseph Fourier.

<sup>§</sup> Nancy University.

<sup>||</sup> IMPMC Campus Boucicaut.

molecules on each side of the interlayer midplane, which hosts cations, in order to properly model the XRD experimental profiles.<sup>20</sup> A Gaussian-shaped distribution of H<sub>2</sub>O molecules about the two main positions further improved the agreement with the high-angle data for dioctahedral and trioctahedral smectites having octahedral and tetrahedral substitutions.<sup>27</sup> In addition, the interlayer water contents determined from XRD profile modeling using such a configuration matched closely those determined from water vapor adsorption/desorption isotherm experiments. This alternate configuration for 2W layers is consistent with the three-dimensional (3D) structure determination of vermiculite minerals,<sup>29–35</sup> and with Monte Carlo simulations.<sup>36–44</sup> For 1W layers, cations and H<sub>2</sub>O molecules are usually located in the interlayer midplane.<sup>28</sup> This configuration allows reproducing 00 $l$  reflections of a variety of dioctahedral smectites saturated with monovalent and divalent cations, without introducing significant positional scatter.<sup>20</sup> Positional disorder of interlayer H<sub>2</sub>O molecules is, however, suggested by the 3D structure refinement of vermiculites,<sup>45–47</sup> and by computational studies.<sup>36,37,40,42,44,48–51</sup>

The present XRD modeling study thus integrates this positional disorder in the determination of the fine interlayer structure of smectite and of its evolution upon dehydration using low- and high-charge synthetic saponites. The water content determined from the modeling procedure is compared to results obtained from water vapor adsorption/desorption isotherms experiments.<sup>52</sup> The influence of specific parameters such as crystallinity, charge distribution, and layer charge amount on the hydration heterogeneity of smectites is also discussed based on the comparison with results obtained on a variety of natural samples by using the same approach.

## Material and Methods

**Samples.** The investigated saponites were prepared at ISTO (Orléans, France) by hydrothermal treatment as described in detail elsewhere,<sup>40</sup> before being sodium saturated.<sup>20</sup> Their structural formulas are the following: Na<sub>*x*</sub>(Si<sub>8–*x*</sub>,Al<sub>*x*</sub>)(Mg<sub>6</sub>)O<sub>20</sub>(OH)<sub>4</sub>, with *x* = 0.8 and 1.4. The two samples are hereafter referred to as S–Na<sub>0.8</sub> and S–Na<sub>1.4</sub>, respectively. The water vapor adsorption/desorption isotherms for the two saponite samples were reported previously.<sup>52</sup> For these experiments, the samples were outgassed at 110 °C for 18 h under a residual pressure of 0.01 Pa. Water vapor was then supplied from a source kept at 45 °C to the samples (thermostated at 30 °C) at a slow flow rate to ensure quasi-equilibrium conditions during the whole experiment.

**X-ray Diffraction in Water Desorption Conditions.** For the two samples, oriented slides were prepared by drying at room temperature a clay slurry on a glass slide. XRD patterns were then recorded with a Bruker D5000 diffractometer equipped with a SolX Si(Li) solid-state detector from Baltic Scientific Instruments, and an Ansyco rh-plus 2250 humidity control device coupled to an Anton Paar TTK450 chamber. Scanning parameters were 0.04° 2 $\theta$  as step size and 6 s as counting time per step over the 2–50° 2 $\theta$  Cu K $\alpha$  angular range. The divergence slit, the two Soller slits, the antiscatter, and resolution slits were 0.5°, 2.3°, 2.3°, 0.5°, and 0.06°, respectively. The experimental setup does not allow vacuum-drying the sample at elevated temperature in situ. It is thus impossible to reproduce the conditions used in adsorption for water vapor isotherms. In contrast, experimental conditions similar to those along the desorption isotherm can be obtained, thus allowing the direct comparison between gravimetric and XRD results. Samples were then first equilibrated at ~92% relative humidity

(RH) and RH was decreased stepwise, with a constant in situ monitoring with a hygrometer (uncertainty of ~2% RH) located near the sample. The position and shape of the 001 reflection were also monitored along the isotherm and complete XRD patterns were collected if significant modifications were observed. Low RH values (<7% RH) were obtained by bubbling a dry gas (~7% RH) into H<sub>2</sub>SO<sub>4</sub> acid solutions at various concentrations. The “dry” state was obtained at the end of each isotherm experiment by outgassing the entire Paar chamber (~10<sup>–4</sup> Pa) at ambient temperature.

**XRD Profile Modeling of 00 $l$  Reflections.** The algorithms developed initially by Sakharov and co-workers were used to fit experimental XRD profiles over the 2–50° 2 $\theta$  Cu K $\alpha$  range with a trial-and-error approach.<sup>53–55</sup> Instrumental and experimental factors such as horizontal and vertical beam divergences, goniometer radius, length, and thickness of the oriented slides were measured and introduced without further adjustment. The mass absorption coefficient ( $\mu^*$ ) was set to 45 cm<sup>2</sup>g<sup>–1</sup>, as recommended.<sup>28</sup> Additional variable parameters include the layer-to-layer distance, which is hereafter referred to as layer thickness, and the coherent scattering domain size (CSDS) along the *c*\* axis, which was characterized by a maximum CSDS value, set to 50 layers, and by a variable mean value (*N*).<sup>56</sup> The layer thickness was allowed to deviate from its mean value by introducing a variance parameter  $\sigma_z$  to account for this “disorder of the second type”.<sup>20,57,58</sup> The *z*-coordinates of all atoms building up the 2:1 layer were set as determined for vermiculite minerals.<sup>35</sup> The interlayer configuration used for 2W layers considers a unique distribution of H<sub>2</sub>O molecules on each side of the interlayer midplane where interlayer cations are located (Debye–Waller parameter  $B = 5 \text{ \AA}^2$ ).<sup>27</sup> This double Gaussian model (2WG) is characterized by the distance ( $\Delta d$ ) between the interlayer midplane and the maximum of the Gaussian distribution. The total number of interlayer H<sub>2</sub>O molecules was also refined together with the full width at half-maximum intensity (fwhm) parameter of the Gaussian distribution. In the present work, the interlayer configuration of 1W layers considers the cations ( $B = 5 \text{ \AA}^2$ ) and H<sub>2</sub>O molecules to be located on the interlayer midplane, H<sub>2</sub>O molecules being normally distributed about this position. The total number of H<sub>2</sub>O molecules and the fwhm of the Gaussian were considered as variable parameters. For 0W layers, Na<sup>+</sup> cations are located also on the interlayer midplane with a *B* parameter of 5 Å<sup>2</sup>.

The fitting procedure was described in detail elsewhere.<sup>25–27,59</sup> Briefly, a main structure, periodic (i.e., with only one type of layer) if possible, is used to reproduce as much as possible of the data. If necessary, additional contributions to the diffracted intensity are introduced to account for the misfit between calculated and experimental patterns. Up to four mixed-layer structures, each with a different composition (relative proportion of the different layer types), were necessary to reproduce the data because of the observed hydration heterogeneity. Note that the use of several mixed-layer structures to fit all features of experimental XRD patterns does not imply the actual presence of different populations of particles in the sample but rather indicates that hydration heterogeneities are not randomly distributed within smectite crystallites.<sup>25–27,59</sup> As a result and for a given XRD pattern, layers with a given hydration state were assumed to have identical parameters (layer thickness and interlayer configuration) in all mixed-layer structures so as to reduce the number of variable parameters. Similarly, *N* and  $\sigma_z$  parameters were considered identical for all mixed-layer structures used to fit a given pattern, although these parameters were varied as a function of RH. The relative proportions of the

different mixed-layer structures and their compositions were also adjusted. The unweighted  $R_p$  parameter was used to assess the overall fit quality because this parameter is mainly influenced by the most intense diffraction maxima such as the 001 reflection, which contains essential information on the proportions of the different layer types and on their respective layer thickness values. The weighted  $R_{wp}$  parameter was used also to assess the overall fit quality.<sup>60</sup> Calculated profiles are shown over the 2–50°  $2\theta$  Cu K $\alpha$  angular range even if a systematic misfit is observed on the low-angle side of the 001 reflection, possibly as the result of an incorrect description of crystalline defects.<sup>20,61</sup> This low-angle region was excluded for the calculation of  $R_p$  and  $R_{wp}$  parameters. Finally, for the sake of simplicity the terms “00 $l$ ” and “001, 002, ...” reflections are used throughout the paper to identify the diffraction maxima, although these correspond to mixed-layer structures and not to periodic structures.

## Results

Calculated and experimental profiles of all samples are shown as a function of relative humidity together with their difference plots in Figure 1. The relative proportions of the different mixed-layer structures and their compositions are reported in Tables 1 and 2 for S–Na<sub>0.8</sub> and S–Na<sub>1.4</sub>, respectively. Tables 1 and 2 also include  $N$ ,  $\sigma_z$ , thickness of 1W and 2W layers, and the parameters describing the interlayer water organization (water content, fwhm of the Gaussian distributions, and  $\Delta d$  parameter for 2W layers). The relative contributions of the different mixed-layer structures to the diffracted intensity and their evolution as a function of RH are illustrated in Figure 2 for characteristic XRD patterns. Finally, the relative proportions of 0W, 1W, and 2W layers are shown as a function of RH for the two samples in Figure 3.

Along the desorption isotherm, XRD patterns recorded for both samples were fitted with two randomly interstratified mixed-layer structures down to ~65% RH (Tables 1 and 2, Figures 1 and 2). The main structure contains only or mostly 2W layers, whereas the second mixed-layer one, which contains the three layer types, allows reproducing the asymmetry on the high-angle side of the 001 peak (Figure 2). With decreasing RH, the more pronounced asymmetry of the 001 peak is reproduced by increasing the proportion of 1W layers at the expense of 2W layers in the two mixed-layer structures (Tables 1 and 2). When decreasing RH below 65%, the overall content of 2W layers decreases below ~90% for both samples (Figure 3), and it is necessary to split the more heterogeneous contribution into two mixed-layer structures (Figure 2). With increasing dehydration, the proportion of 2W layers in these two structures decreases (Tables 1 and 2). Three mixed-layer structures allow reproducing the evolution of XRD profiles down to an overall content of 2W layers of ~70% (Figure 3). For lower contents of 2W layers, hydration heterogeneity is further increased and additional peaks corresponding to essentially monohydrated smectite are visible in addition to 00 $l$  reflections of 2W smectite. For instance, the XRD pattern recorded at 42% RH for S–Na<sub>1.4</sub> exhibits a 002 smectite peak at ~14°  $2\theta$  (Figure 2), which requires a fourth mixed-layer structure dominated by 1W layers. Four mixed-layer structures were consistently used to fit XRD profiles exhibiting 00 $l$  reflections of both 1W and 2W smectite (Figures 1 and 2; 52–46% and 42–23% RH range for S–Na<sub>0.8</sub> and S–Na<sub>1.4</sub>, respectively). When the 2W–1W transition is essentially complete, XRD profiles exhibit a main 001 reflection corresponding to 1W smectite but asymmetric on its low-angle side. Such profiles are fitted with three or two mixed-layer

structures, as the overall content of 1W layers increases (Figures 1–3, Tables 1 and 2). 1W layers prevail over the 32–8% and 16–4% RH ranges for S–Na<sub>0.8</sub> and S–Na<sub>1.4</sub>, respectively (Figure 3). Hydration heterogeneity increases again during the 1W–0W transition, thus requiring to increase again the number of mixed-layer contributions (Tables 1 and 2, Figures 1 and 2). The experimental pattern recorded at ~0% RH for S–Na<sub>1.4</sub> was reproduced assuming three randomly interstratified mixed-layer structures with contrasting 0W:1W ratios (Table 2, Figure 1). XRD profiles obtained for S–Na<sub>0.8</sub> at 2 and ~0% RH exhibit a specific hump at ~4.5°  $2\theta$  (Figures 1 and 2) typical of the ordered interstratification of 1W and 0W layers (maximum possible degree of ordering, R1-MPDO). Such a R1-MPDO mixed-layer structure contributes ~16% of the total intensity (2% RH, Table 1) but allows reproducing both the low-angle hump and additional reflections at ~16° and ~24°  $2\theta$  (Figure 2).

## Discussion

**Structural Features of Saponite.** Using a systematic fitting procedure the evolution of layer type abundance and of crystal parameters can be followed accurately along the water vapor desorption isotherm, which allows assessing the specificity of the studied saponite by comparison with previous studies performed on natural smectites.<sup>20,25,26</sup>

**Structure Models and Crystal Parameters Evolution.** The CSDSs along the  $c^*$  axis ( $N$  parameter, Tables 1 and 2) are higher for saponites than for natural smectites.<sup>20,25,26</sup> Such CSDS values indicate a better crystallinity of the present saponites likely in relation with their synthetic origin. In addition, during the 2W–1W transition, the  $N$  values increase from 12.5 to 14.0 and from 12.0 to 15.0 layers for S–Na<sub>0.8</sub> and S–Na<sub>1.4</sub>, respectively (Tables 1 and 2). The  $N$  values increase further during the 1W–0W transition from 14 to 18 layers and from 15 to 17 layers for S–Na<sub>0.8</sub> and S–Na<sub>1.4</sub>, respectively. A similar CSDS increase with decreasing hydration was already observed as a result of either RH decrease or temperature increase.<sup>20,25,26</sup> It was interpreted as a disruption of some 2W layer stacks owing to weaker electrostatic interactions between layers resulting from increasing interlayer distances upon hydration. Although consistent with this interpretation, the CSDS increase during the 2W–1W transition is less significant than that for Na-saturated low-charge montmorillonite (increase of ~25% and ~50%, respectively).<sup>20</sup> The same is valid for the 1W–0W transition. This reduced effect could result from (i) a larger CSDS characterized here in the  $c^*$  direction but likely also in the ( $a,b$ ) plane due to the synthesis protocol and (ii) the localization of charge deficit in the tetrahedra. Both effects likely contribute to increase the overall layer–cation–layer attraction forces between adjacent layers for most hydrated states.

The evolution with relative humidity of the  $\sigma_z$  parameter, which characterizes the fluctuation of layer thickness, displays similar trends when comparing saponites and Na-saturated low-charge montmorillonite.<sup>20</sup> The  $\sigma_z$  values are similar when either 0W or 2W layers prevail, and are higher for mostly monohydrated structures. Such a feature, though not fully understood, then appears as a signature of smectite exchanged with monovalent cations. Indeed for smectite saturated with divalent cations (Ca<sup>2+</sup>, Sr<sup>2+</sup>, Mg<sup>2+</sup>) an increase of  $\sigma_z$  values is systematically observed for bihydrated states.<sup>20,25,26</sup> In the case of saponite, an increase of layer charge appears to slightly lower the value of  $\sigma_z$  when 1W layers prevail (0.28 and 0.21 Å for S–Na<sub>0.8</sub> and S–Na<sub>1.4</sub> samples, respectively; Tables 1 and 2). This may



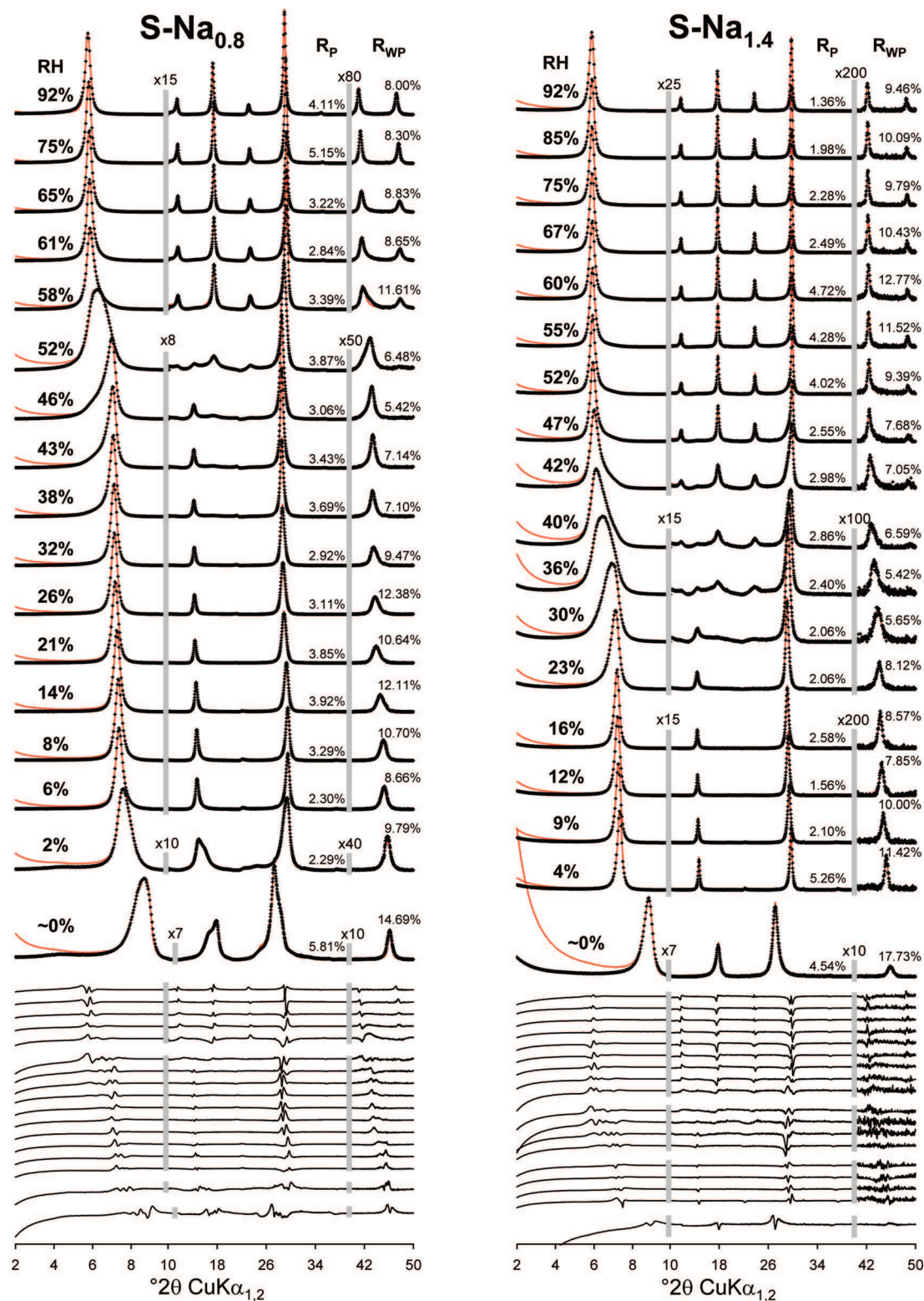


**Figure 1.** Comparison between experimental and calculated XRD patterns as a function of RH for S-Na<sub>0.8</sub> (left) and S-Na<sub>1.4</sub> (right). Experimental and calculated XRD patterns are shown as crosses and solid lines, respectively. Difference plots are shown at the bottom of the figure. The vertical gray bars indicate a modified scale factor for the high-angle regions compared to the 2–10° 2θ angular range. The goodness of fit parameters ( $R_p$  and  $R_{wp}$ ) are indicated for each pattern.

tentatively be assigned to stronger cation–layer interactions but additional studies are required to confirm such an assumption.

**Hydration: Evolution and Heterogeneity.** When looking at the evolution of layer abundance along the water vapor desorption isotherm (Figure 3), plateaus are observed for 2W and 1W states. On these plateaus the proportion of a given layer type exceeds 95%, thus indicating a very low hydration

heterogeneity whereas the proportion of a given layer type seldom exceeds 90% for natural montmorillonites and beidelites.<sup>20,26</sup> The observed reduced hydration heterogeneity is likely induced by a homogeneous distribution of tetrahedral charges involving in turn a homogeneous distribution of interlayer cations. Still, 0W layers (with 9.8 Å layer thickness) are present all along the isotherm for the two samples, as systematically

**TABLE 1: Structural Parameters Used To Reproduce Experimental Patterns of S-Na<sub>0.8</sub> as a Function of RH**

RH (%)	S cont. (%) <sup>a</sup>	2W/1W/0W <sup>b</sup>	LT 2W <sup>c</sup>	nH <sub>2</sub> O 2W <sup>d</sup>	fwhm H <sub>2</sub> O 2W <sup>e</sup>	$\Delta d(2W)^f$	LT 1W <sup>c</sup>	nH <sub>2</sub> O 1W <sup>d</sup>	fwhm H <sub>2</sub> O 1W <sup>e</sup>	N <sup>g</sup>	$\sigma_z^h$	total 2W/1W/0W <sup>i</sup>
92	51	100/0/0-R0	15.40	9.60	1.37	1.42	13.10	6.00	2.50	12.5	0.16	95.1/3.4/1.5
	49	90/7/3-R0										
75	73	99/1/0-R0	15.29	9.30	1.35	1.33	12.90	5.60	2.30	12.5	0.18	95.2/3.2/1.6
	27	85/9/6-R0										
65	72	97/3/0-R0	15.23	9.24	1.32	1.32	12.80	5.40	2.15	12.5	0.21	91.2/7.2/1.7
	28	76/18/6-R0										
61	52	96/4/0-R0	15.22	9.20	1.32	1.31	12.73	5.30	2.05	13.0	0.21	86.4/11.2/2.4
	30	85/12/3-R0										
	18	62/30/8-R0										
58	38	96/4/0-R0	15.21	9.10	1.32	1.30	12.70	5.25	1.95	13.0	0.23	75.8/21.9/2.4
	38	75/25/0-R0										
	24	45/45/10-R0										
52	18	83/15/2-R0	15.14	9.00	1.30	1.30	12.57	4.95	1.82	13.0	0.23	48.0/49.3/2.6
	47	54/42/4-R0										
	27	26/74/0-R0										
46	8	5/90/5-R0	15.10	8.90	1.30	1.30	12.53	4.90	1.80	13.0	0.25	17.9/79.6/2.5
	3	84/14/2-R0										
	7	60/40/0-R0										
43	29	28/70/2-R0	15.08	8.80	1.25	1.28	12.51	4.90	1.78	13.0	0.25	12.2/85.1/2.7
	61	5/92/3-R0										
	6	65/33/2-R0										
38	28	26/72/2-R0	15.05	8.76	1.25	1.28	12.50	4.85	1.78	14.0	0.25	6.6/90.5/2.9
	66	2/95/3-R0										
	3	65/33/2-R0										
32	11	26/72/2-R0	15.01	8.60	1.25	1.28	12.46	4.80	1.72	14.0	0.28	1.6/95.1/3.3
	86	2/95/3-R0										
	84	0/98/2-R0										
26	16	10/80/10-R0	15.01	8.60	1.25	1.28	12.46	4.80	1.72	14.0	0.28	1.6/95.1/3.3
	81	0/98/2-R0										
21	19	0/90/10-R0	15.01	8.60	1.25	1.28	12.46	4.80	1.72	14.0	0.28	1.6/95.1/3.3
	93	0/93/7-R0										
14	7	0/80/20-R0	15.01	8.60	1.25	1.28	12.46	4.80	1.72	14.0	0.28	1.6/95.1/3.3
	87	0/97/3-R0										
	13	0/80/20-R0										
8	67	0/97/3-R0	15.01	8.60	1.25	1.28	12.46	4.80	1.72	14.0	0.28	1.6/95.1/3.3
	33	0/80/20-R0										
6	53	0/96/4-R0	15.01	8.60	1.25	1.28	12.46	4.80	1.72	14.0	0.28	1.6/95.1/3.3
	10	0/40/60-R0										
	37	0/15/85-R0										
2	20	0/90/10-R0	15.01	8.60	1.25	1.28	12.46	4.80	1.72	14.0	0.28	1.6/95.1/3.3
	41	0/75/25-R1										
	16	0/63/37-R1										
0	23	0/40/60-R0	15.01	8.60	1.25	1.28	12.46	4.80	1.72	14.0	0.28	1.6/95.1/3.3
	13	0/55/45-R0										
	14	0/38/62-R1										
	34	0/20/80-R1	15.01	8.60	1.25	1.28	12.46	4.80	1.72	14.0	0.28	1.6/95.1/3.3
	39	0/6/94-R1										

<sup>a</sup> Relative proportion of the different contributions to the diffracted intensity. <sup>b</sup> Relative proportions of the different layer types in these contributions. 2W, 1W, and 0W stand for bihydrated, monohydrated, and dehydrated layers, respectively. R0 and R1 describe mixed-layer structures with random interstratification or with maximum possible degree of ordering (nearest neighbor ordering), respectively. <sup>c</sup> Layer thickness (LT in Å) for hydrated layers. <sup>d</sup> Number of H<sub>2</sub>O molecules for hydrated layers (per O<sub>20</sub>(OH)<sub>4</sub>). <sup>e</sup> Width of the interlayer H<sub>2</sub>O molecule Gaussian distribution (fwhm in Å). <sup>f</sup> Distance, in projection along the *c*\* axis, between the interlayer midplane and the maximum density of the H<sub>2</sub>O molecule distribution ( $\Delta d$  in Å) for 2W layers. <sup>g</sup> Mean size of the coherent scattering domains along the *c*\* axis (in layers). <sup>h</sup> Standard deviation layer thickness (in Å). <sup>i</sup> Relative contribution of the different layer types.

reported for dioctahedral smectites with contrasting layer charge and charge location. For natural samples, the presence of collapsed layers or dehydrated layers is likely related to the heterogeneous charge distribution.<sup>26</sup> This heterogeneity is expected to be much reduced for synthetic saponites and the number of 0W layers is accordingly extremely low (<2% between 92% and 4% RH for S-Na<sub>1.4</sub>, and <3% between 92% and 38% RH for S-Na<sub>0.8</sub>; Tables 1 and 2).

Despite the low heterogeneity of layer charge distribution in synthetic saponites, the transition from the bihydrated state to the monohydrated states systematically extends over a large relative humidity range (~30 and ~40% RH for samples

S-Na<sub>0.8</sub> and S-Na<sub>1.4</sub>, respectively; Figure 3). As the layer charge distribution in these samples is rather homogeneous, the presence of large RH domains for which important hydration heterogeneity is noticed should be assigned to local thermodynamical effects. Indeed, the transition from one hydration state to the other is associated to the cross of a free-energy barrier.<sup>62,63</sup> As a result, any contrasted structural feature among the different layers may affect the system locally and its ability to cross this free-energy barrier or to remain in a metastable state. The possible statistical distribution of water content that may lead some interlayers to have slightly different water content could be one of the causes of the transition of hydrated layers at

**TABLE 2: Structural Parameters Used To Reproduce Experimental Patterns of S-Na<sub>1,4</sub> as a Function of RH<sup>a</sup>**

RH (%)	S cont. (%)	2W/1W/0W	LT 2W	nH <sub>2</sub> O 2W	fwhm H <sub>2</sub> O 2W	$\Delta d(2W)$	LT 1W	nH <sub>2</sub> O 1W	fwhm H <sub>2</sub> O 1W	N	$\sigma_z$	total 2W/1W/0W
92	92	100/0/0-R0	15.00	9.80	0.90	1.36	13.05	6.00	2.40	12	0.16	97.6/1.6/0.8
	8	70/20/10-R0										
85	88	100/0/0-R0	15.00	9.80	0.90	1.35	12.90	5.90	2.25	12	0.15	96.4/2.4/1.2
	12	70/20/10-R0										
75	87	100/0/0-R0	14.98	9.80	0.90	1.34	12.80	5.70	2.10	12	0.16	96.1/2.6/1.3
	13	70/20/10-R0										
67	83	100/0/0-R0	14.97	9.70	0.90	1.34	12.73	5.50	2.00	12	0.16	94.9/3.4/1.7
	17	70/20/10-R0										
60	75	100/0/0-R0	14.96	9.60	0.90	1.33	12.68	5.45	1.95	12	0.15	91.1/7.3/1.6
	11	80/20/0-R0										
	14	45/40/15-R0										
55	71	100/0/0-R0	14.94	9.56	0.90	1.33	12.65	5.40	1.90	12	0.16	88.7/9.6/1.7
	17	75/25/0-R0										
	12	40/45/15-R0										
52	64	100/0/0-R0	14.93	9.50	0.90	1.32	12.60	5.30	1.85	12	0.17	85.4/13.2/1.4
	22	75/25/0-R0										
	14	35/55/15-R0										
47	65	96/4/0-R0	14.93	9.40	0.90	1.30	12.52	5.10	1.75	12	0.17	79.5/18.7/1.8
	17	70/30/0-R0										
	18	30/60/10-R0										
42	40	90/10/0-R0	14.92	9.30	0.90	1.30	12.49	5.00	1.70	12	0.17	64.9/33.2/1.9
	23	70/30/0-R0										
	30	40/55/5-R0										
	7	15/80/5-R0										
40	17	88/12/0-R0	14.90	9.20	0.90	1.28	12.42	4.90	1.65	12	0.17	52.5/46.0/1.5
	35	65/35/0-R0										
	38	36/62/2-R0										
	10	8/85/7-R0										
36	16	78/22/0-R0	14.89	9.10	0.90	1.28	12.38	4.80	1.60	13	0.19	38.7/59.9/1.4
	34	50/50/0-R0										
	31	26/74/0-R0										
	20	8/85/7-R0										
30	9	60/40/0-R0	14.89	9.00	0.90	1.28	12.32	4.70	1.55	15	0.19	21.8/75.9/1.9
	40	30/70/0-R0										
	23	10/90/0-R0										
	27	8/85/7-R0										
23	3	50/50/0-R0	14.87	8.80	0.90	1.28	12.31	4.70	1.50	15	0.19	9.2/89.3/1.5
	27	20/80/0-R0										
	45	6/94/0-R0										
	25	0/95/5-R0										
16	90	0/100/0-R0	14.86	8.60	0.90	1.28	12.27	4.50	1.45	15	0.21	1.0/98.0/1.0
	10	10/80/10-R0										
12	94	0/100/0-R0					12.22	4.40	1.40	15	0.21	0.0/98.6/1.4
	6	0/80/20-R0										
9	94	0/100/0-R0					12.15	4.25	1.35	15	0.21	0.0/98.6/1.4
	6	0/80/20-R0										
4	96	0/100/0-R0					12.03	3.80	1.20	15	0.21	0.0/98.8/1.2
	4	30/70/0-R0										
~0	15	0/15/85-R0					11.95	3.5	1.00	16	0.19	0.0/6.3/93.7
	67	0/6/94-R0										
	18	0/0/100-R0										

<sup>a</sup> Notations and labels as in Table 1.

different RH values.<sup>64</sup> Still, additional studies involving spectroscopic and computational methods are necessary to fully test such an assumption.

Finally, the 1W–0W transition of S–Na<sub>0,8</sub> is associated with the presence of ordered mixed-layer structures composed of 1W and 0W layers (Figures 1 and 2, Table 1). Similar mixed-layer structures possibly exist also for the high-charge sample, but the 1W–0W transition was not reached for this sample (Figure 3). Similar ordered mixed-layer structures have already been reported upon dehydration of Na- and Sr-saturated low-charge dioctahedral montmorillonite.<sup>20,65</sup> Ordering was interpreted as resulting from the presence of octahedral vacancies leading to a specific orientation of hydroxyl groups.<sup>65</sup> The collapse of smectite interlayer and the insertion of the interlayer cation into

the ditrigonal cavity make the OH group lean toward the vacant octahedral site, thus preventing a similar orientation of the OH group located on the other side of the octahedral sheet and the associated collapse of adjacent interlayer space. In saponite, all octahedral sites are occupied by Mg atoms, and OH groups are perpendicular to the clay layer. An OH tilt resulting from the insertion of interlayer cations into the ditrigonal cavity is thus unlikely. In addition, the interaction between OH groups located on either side of the octahedral sheet is likely negligible because of the absence of vacant octahedra. For saponite, the origin of the observed ordered structure should rather be interpreted as resulting from the rotation of adjacent layers in the (*a,b*) plane. To collapse smectite interlayers, the ditrigonal cavities of adjacent layers have indeed to face each other through layer



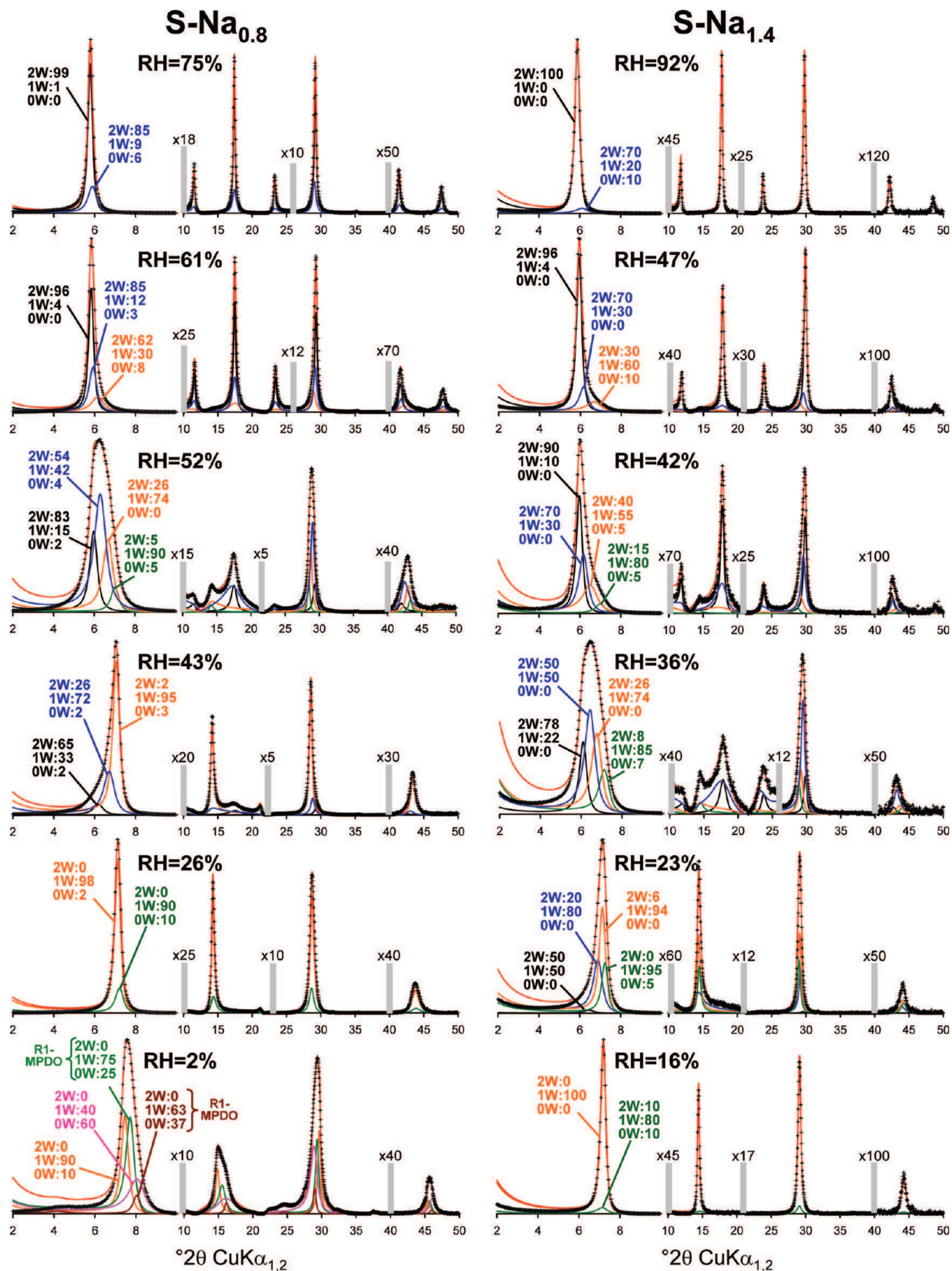


**Figure 2.** Respective contributions of the various mixed-layer structures to the calculated profiles for selected patterns of S-Na<sub>0.8</sub> (left) and S-Na<sub>1.4</sub> (right). Patterns and notations as in Figure 1.



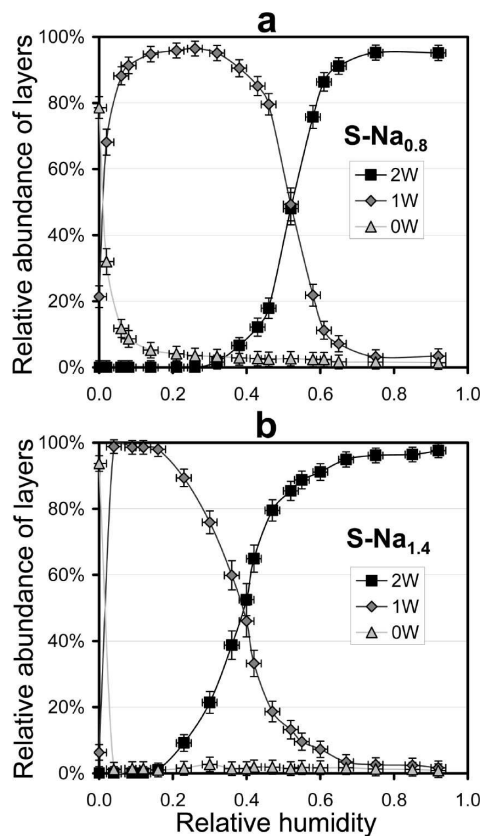


**Figure 3.** Evolution of the relative contribution of the different layer types (summing up all mixed-layer structures) along water vapor desorption isotherms for S-Na<sub>0.8</sub> (a) and S-Na<sub>1.4</sub> (b). Open triangles, gray diamonds, and solid squares represent 0W, 1W, and 2W layers, respectively. The error on RH was estimated to be  $\pm 2\%$ . That on layer abundance was considered to vary linearly from  $\pm 2\%$  when the relative proportion of a given layer is 100% or 0% to  $\pm 5\%$  when this layer represents 50% of the total layers.<sup>25</sup>

rotation, as shown by wetting-and-drying experiments.<sup>66,67</sup> Once such a configuration is obtained for a given interlayer, extending such a configuration to the adjacent interlayer is energetically less favorable. It indeed requires either the mutual rotation of a 2-layer unit and of an individual layer, or a more important rotation of this latter individual layer. According to such an interpretation, the formation of 0W–1W layer pairs will be favored, which could in turn explain the observed stacking order. In such a framework, structural parameters such as the extension of the layer in the (*a,b*) plane, the layer charge, and the nature of the interlayer cation should strongly influence the appearance of such specific layer stacking because of their contrasted influence on the interaction between adjacent layers.

**Organization of Smectite Interlayers.** As discussed above, the hydration behavior of synthetic saponites is similar to that of natural smectites, with, however, a reduced heterogeneity. Synthetic saponites are thus relevant analogues for a detailed investigation of the evolution of smectite interlayer structure as a function of relative humidity. Specifically, the evolution in thickness of the different layer types and the parameters defining the distribution of H<sub>2</sub>O molecules (fwhm and content) can be thoroughly analyzed. For both saponites, the 2W and 1W layers decrease in thickness upon water desorption (Figure 4a,b), as already observed on natural smectites.<sup>20,25,26</sup> This decrease in layer thickness results from the decreasing number of interlayer H<sub>2</sub>O molecules (Figure 4b).

**Dehydrated Layers.** 0W layers were considered to have a constant thickness of 9.8 Å throughout the whole RH range.

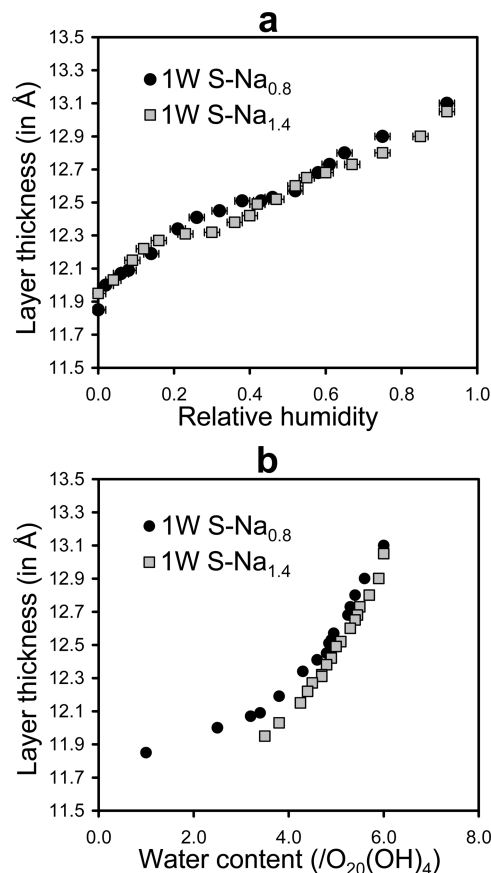


**Figure 4.** Evolution of monohydrated layer thickness as a function of (a) relative humidity and (b) interlayer water content. Solid circles and gray squares represent results obtained for S-Na<sub>0.8</sub> and S-Na<sub>1.4</sub>, respectively.

This value, higher than that determined previously for natural Na-saturated montmorillonite (9.6 Å),<sup>20</sup> is consistent with the increased thickness of trioctahedral 2:1 layers (6.69 Å) compared to dioctahedral ones (6.54 Å).<sup>28,35</sup> For 0W layers, the interlayer cation is assumed to be located on the interlayer midplane with a Debye–Waller *B* parameter of 5 Å<sup>2</sup>. This model is not fully consistent with the observed perturbation of the layer hydroxyl vibration mode that pleads for interlayer cations located closer to the 2:1 layer surface.<sup>68</sup> XRD is, however, weakly sensitive to the interlayer cations owing to their low content, and computational approaches are likely more appropriate to accurately determine the actual configuration of interlayer cations in 0W layers.

**Monohydrated Layers.** For 1W layers, the evolution of layer thickness upon dehydration is similar for the two samples, thus indicating that the number of interlayer cations does not significantly influence their collapse (Figure 4a). However, for similar thickness values, the water contents are different between the two saponites, S-Na<sub>1.4</sub> hosting more H<sub>2</sub>O molecules for a given basal distance (Figure 4b). In addition, for low water contents (<4–4.5 H<sub>2</sub>O/O<sub>20</sub>(OH)<sub>4</sub>; Figure 4b) a slope change can be noticed at RH = 14% for S-Na<sub>0.8</sub> (Table 1). Such slope change, that may be present as well for S-Na<sub>1.4</sub>, indicates that for water contents below  $\sim 4$  H<sub>2</sub>O/O<sub>20</sub>(OH)<sub>4</sub>, the effect of dehydration on interlayer spacing is more limited. This water amount corresponds for both samples to the threshold limit below which the 1W–0W transition starts occurring (Figure 3a). It may then be assumed that below this value, the remaining H<sub>2</sub>O molecules are all interacting with the interlayer cation, probably forming its first hydration shell. This water content

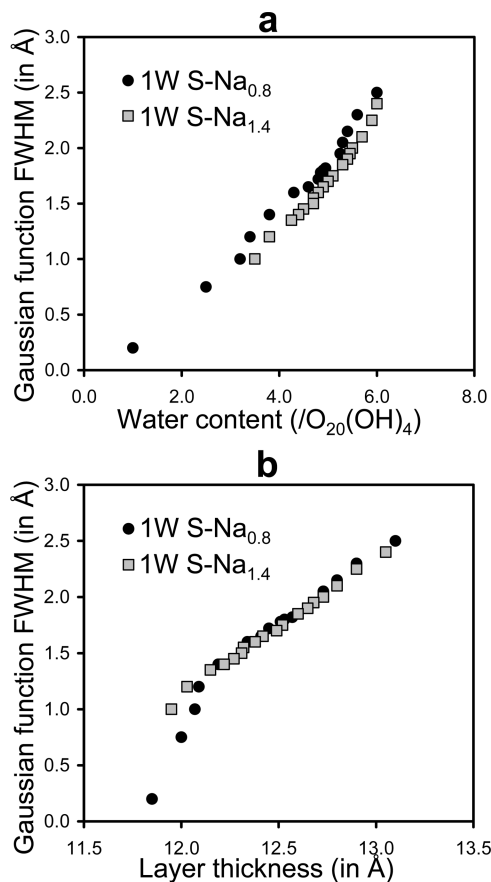


**Figure 5.** Evolution of the fwhm of the H<sub>2</sub>O molecule Gaussian distribution about the interlayer midplane for 1W layers as a function of (a) interlayer water content and (b) layer thickness. Symbols as in Figure 4.

corresponds to  $\sim 5$  and  $\sim 3$  H<sub>2</sub>O molecules per cation for the low- and high-charge saponite, respectively, in agreement with results obtained by Rinnert et al.<sup>40</sup> on similar samples. These values are also consistent with the three-dimensional (3D) structure determination obtained for Ca-, Sr-, Li-, Ba-, or Na-saturated vermiculite minerals in which the cation hydration shell was found to not exceed 4 H<sub>2</sub>O molecules per cation with a coordination similar to a flat tetrahedron.<sup>45–47,69–71</sup>

Additional information can be obtained by examining the evolution of the interlayer water configuration, as seen through the width of the Gaussian distribution of water molecules located close to the midplane of the interlayer space (fwhm, Tables 1 and 2). Figure 5a displays the evolution of fwhm values as a function of water content. For both samples a positive linear correlation is obtained, indicating an increase of the positional disorder of H<sub>2</sub>O molecules with increasing water content. In contrast, plotting the same parameter as a function of layer thickness (Figure 5b) reveals a slope change for both samples corresponding to the onset of the 1W–0W transition, i.e., when all remaining H<sub>2</sub>O molecules contribute to the hydration shell of the interlayer cation. In this regime, the low fwhm values and the marginal effect of dehydration on layer thickness are consistent with a planar arrangement of H<sub>2</sub>O molecules surrounding sodium cation, similar to that evidenced for vermiculite minerals.<sup>45–47,69–71</sup>

**Bihydrated Layers.** The evolution in thickness of 2W layers as a function of relative humidity (Figure 6a) is correlated also to the water content (Figure 6b). The two samples, however, exhibit strongly contrasting behaviors, the layer thickness variation being much more important for S–Na<sub>0.8</sub> than for

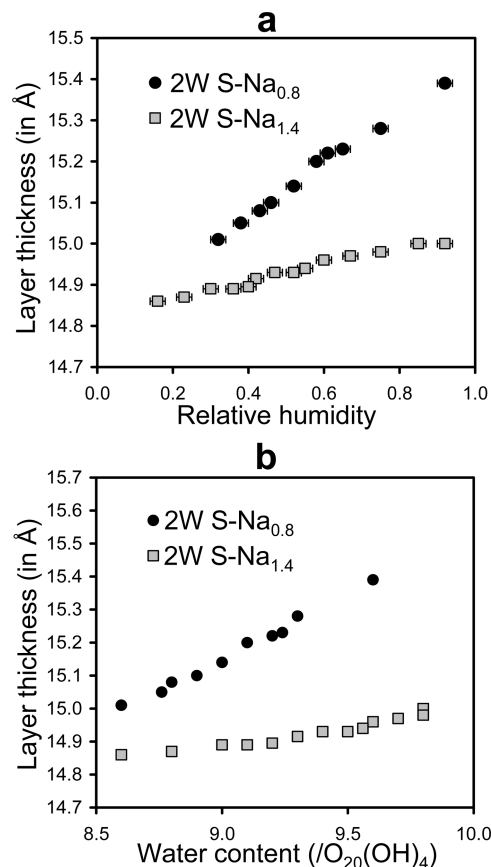


**Figure 6.** Evolution of bihydrated layer thickness as a function of (a) relative humidity and (b) interlayer water content. Symbols as in Figure 4.

S–Na<sub>1.4</sub> and the high-charge sample having systematically a smaller thickness for a given water content. For S–Na<sub>0.8</sub>, the fwhm of the interlayer H<sub>2</sub>O Gaussian distribution decreases (from 1.37 to 1.25 Å for RH = 92% and 32% respectively; Table 1) together with the distance  $\Delta d(2W)$  between the interlayer midplane and the maximum of the distribution (from 1.42 to 1.28 Å for RH = 92% and 32% respectively; Table 1). In contrast, the fwhm of the interlayer H<sub>2</sub>O Gaussian distribution is constant at 0.90 Å for S–Na<sub>1.4</sub>, and  $\Delta d(2W)$  values decrease only slightly with decreasing RH (from 1.36 to 1.28 Å for RH = 92% and 16% respectively; Table 2). The decrease in fwhm values for S–Na<sub>0.8</sub> is consistent with previous reports on natural smectites<sup>27</sup> and can be attributed to the removal of H<sub>2</sub>O molecules weakly bound to the cation. The H<sub>2</sub>O molecules bound to the cation likely have a more constrained *z*-position, as evidenced by the narrower distributions of H<sub>2</sub>O molecules, despite a higher water content, displayed by S–Na<sub>1.4</sub> for a given layer thickness (for example, 32% and 92% RH for S–Na<sub>0.8</sub> and S–Na<sub>1.4</sub>, respectively; Tables 1 and 2). This effect likely results from the increased number of interlayer cations and the stronger undersaturation of surface oxygen atoms when increasing the layer charge deficit. Both features favor the formation of a well-defined network of H<sub>2</sub>O molecules in the interlayer space, as confirmed by the lower layer thickness values determined for S–Na<sub>1.4</sub> and by vibrational spectroscopy.<sup>68</sup> The evolution of  $\Delta d(2W)$  values determined for the two samples is likely related to a balance between H<sub>2</sub>O molecules interactions with interlayer cations and the 2:1 layer surface. Such a hypothesis is supported by the constant ratio between  $\Delta d(2W)$  and the distance between interlayer midplane and the 2:1 layer

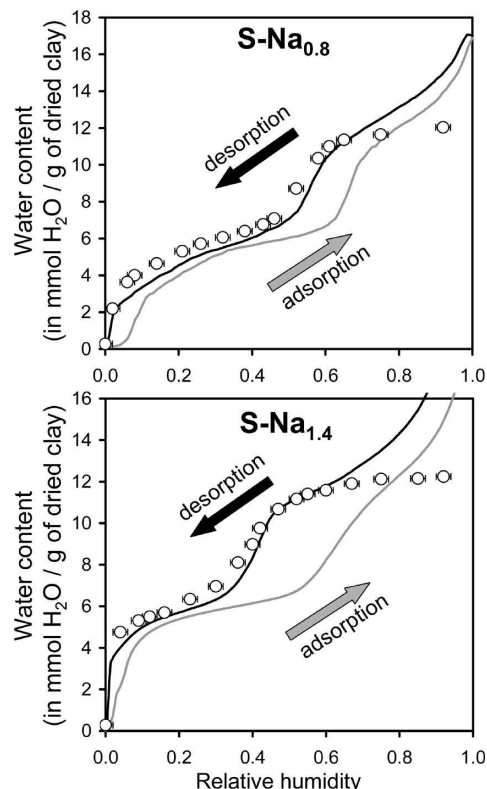


**Figure 7.** Comparison of the water contents derived from XRD profile modeling (eq 1; open circles) with those determined from water vapor adsorption/desorption isotherms.<sup>52</sup> Adsorption and desorption pathways are shown as gray and solid lines, respectively.

surface ( $31(\pm 1)\%$  and  $32(\pm 1)\%$  for S-Na<sub>0.8</sub> and S-Na<sub>1.4</sub>, respectively).

**Influence of Layer Charge on Saponite Hydration.** As discussed above, the two samples display contrasting hydration heterogeneities and interlayer water organization. Along the water vapor desorption isotherm, the transitions between hydration states are shifted toward lower RH values when increasing the layer charge (Figure 3), consistent with previous results obtained on an extended set of saponites,<sup>72</sup> and on natural dioctahedral smectites.<sup>26</sup> An increase in layer charge increases the numbers of interlayer cations, and thus the total hydration enthalpy. As a result, the number of H<sub>2</sub>O molecules bound to interlayer cations increases at the expense of weakly bound H<sub>2</sub>O molecules. The formation of an interlayer H<sub>2</sub>O molecules network allows lower layer thickness values for S-Na<sub>1.4</sub> compared to S-Na<sub>0.8</sub>, despite a higher number of H<sub>2</sub>O molecules (Figures 4b and 6b). It enhances the cohesion between adjacent layers as evidenced by an increase of *N* values (Tables 1 and 2), thus increasing the stability of most hydrated layers toward lower RH values for higher layer charge (Figure 3). The reduced thickness observed for 2W layers of S-Na<sub>1.4</sub> appears to be typical of saponites as this parameter is almost independent of layer charge for natural dioctahedral smectites.<sup>26</sup> The ordering of Al-for-Si isomorphous substitutions, which is thought to favor the ordering of interlayer cation distribution in vermiculites,<sup>26</sup> has been reported also for high-charge S-Na<sub>1.4</sub>.<sup>72</sup>

**Distribution Balance of Different Types of Water.** The water contents derived from XRD profile modeling and those obtained from water vapor adsorption/desorption isotherms are compared in Figure 7 for S-Na<sub>0.8</sub> and S-Na<sub>1.4</sub>. The water amount  $Q_{\text{H}_2\text{O}}$  (in moles of H<sub>2</sub>O per gram of dried clay) is calculated by using the following equation:

$$Q_{\text{H}_2\text{O}} = \sum_{i=1}^2 [n\text{H}_2\text{O}^{\text{iW}} \times Ab^{\text{iW}}] / m_{\text{clay}} \quad (1)$$

where  $n\text{H}_2\text{O}^{\text{iW}}$  and  $Ab^{\text{iW}}$  correspond respectively to the water content per O<sub>20</sub>(OH)<sub>4</sub> and to the relative abundance of a given *i*-hydrated layer (i.e., 1W or 2W layer). This content is divided by the molar mass of a unit cell of dry clay  $m_{\text{clay}}$ , that is 776 and 789 g for S-Na<sub>0.8</sub> and S-Na<sub>1.4</sub>, respectively. The water contents and the RH values corresponding to the 2W–1W and 1W–0W transitions determined by using the two methods are consistent (Figure 7). However, the  $Q_{\text{H}_2\text{O}}$  values derived from XRD modeling are slightly higher than those obtained from water vapor desorption gravimetry over the 0–60% RH range and significantly lower at high RH values (Figure 7). At high RH values the two methods do not probe the same H<sub>2</sub>O molecules: XRD is sensitive only to crystalline water, which is located in smectite interlayers, whereas gravimetry experiments measure also H<sub>2</sub>O molecules located on external smectite surfaces or in meso- and macropores. Over the 92–60% RH range, the relative intensities and positions of 00*l* reflections are not significantly modified (Figure 1, Tables 1 and 2). The additional water determined by gravimetry over this RH range thus likely corresponds to the water sorption on external surfaces and in wedge-shaped meso- and macropores as suggested previously for montmorillonites.<sup>21–23</sup> For lower RH values, the observed difference (Figure 7) could arise from the uncertainty of the XRD procedure. However, some H<sub>2</sub>O molecules subsist in the outgassing conditions prior to the gravimetry experiments (110 °C, residual pressure of 0.01 Pa).<sup>52</sup> The water contents determined by the two methods can be reconciled assuming residual water contents of 0.60 and 0.45 mmol of H<sub>2</sub>O per g of dry clay for S-Na<sub>0.8</sub> and S-Na<sub>1.4</sub>, respectively, thus shifting experimental isotherms (Figure 8). These values are consistent with previous reports on the same samples.<sup>52</sup> From this unified description, the relative contents of crystalline and pore water can be determined (Figure 8).

## Conclusions

XRD profile modeling has proven successful for quantifying the structural evolution of synthetic saponites upon dehydration. Accurate profile modeling can only be achieved by assuming positional disorder of water molecules around one or two positions for mono- or bihydrated layers, respectively. Such a vision, that provides water amount consistent with those determined from water vapor desorption isotherms, allows finely assessing the effect of layer charge on the interlayer water organization. Increased layer charge leads to the formation of a more structured water network and shifts hydration transitions toward lower relative humidity conditions. Additionally the modeling procedure allows discriminating the different types of H<sub>2</sub>O molecules present in smectites in unsaturated water vapor conditions (Figure 8). This is crucial for understanding the reactivity of smectites toward water in natural media, as the dynamical properties of H<sub>2</sub>O molecules strongly depend on their binding strength with respect to the clay layers.

Still, many questions remain open regarding the actual coordination between H<sub>2</sub>O molecules and interlayer cations, the influence on the organization of interlayer H<sub>2</sub>O molecules of factors such as (i) the orientation of H<sub>2</sub>O molecules taking into account hydrogen atoms, (ii) the layer stacking, and (iii) the layer extension in the (*a,b*) plane. Because of the insensitivity of X-ray toward hydrogen atoms, information about hydrogen atoms organization could be obtained by performing structural



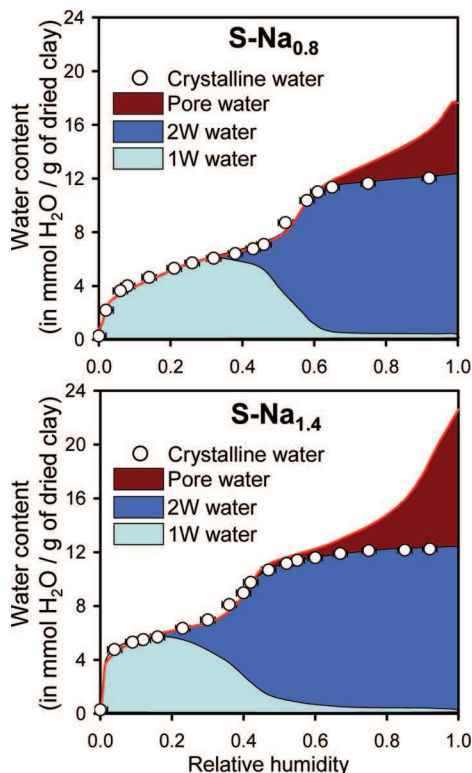


**Figure 8.** Relative contributions of the different types of H<sub>2</sub>O molecules along the water vapor desorption isotherm. The total water content determined from gravimetric experiments is corrected for the presence of residual water (see text for details). The contribution of water in meso- and/or macropores is calculated as the difference between the total water content and the contribution of crystalline water present in 1W and 2W interlayers.

analyses based on neutron diffraction experiments. In parallel, the discrimination between water molecules differently coordinated to the interlayer cation could be best revealed by numerical Monte Carlo simulations. The second part of the present series of papers will then be specifically devoted to a thorough confrontation between computational approaches and experimental diffraction data.

**Acknowledgment.** Nicolas Geoffroy (LGCA, Grenoble) is thanked for assistance during XRD analysis. E.F. gratefully acknowledges financial support from a European Marie-Curie Reintegration grant (contract no. MERG-CT-2007-046413) and from a French ANR “Jeunes Chercheurs” program (contract no. JC09\_462986-PorousClay). The paper was improved by the constructive comments of two anonymous reviewers.

## References and Notes

- (1) Laird, D. A.; Barak, P.; Nater, E. A.; Dowdy, R. H. *Soil Sci. Soc. Am. J.* **1991**, *55*, 1499.
- (2) Burst, J. F. *Am. Assoc. Pet. Geol. Bull.* **1969**, *53*, 73.
- (3) Freed, R. L.; Peacor, D. R. *Am. Assoc. Pet. Geol. Bull.* **1989**, *73*, 1223.
- (4) Brown, K. M.; Ransom, B. *Geology* **1996**, *24*, 843–846.
- (5) Boutareaud, S.; Calugaru, D. G.; Han, R.; Fabbri, O.; Mizoguchi, K.; Tsutsumi, A.; Shimamoto, T. *Geophys. Res. Lett.* **2008**, *35*.
- (6) Boullier, A. M.; Yeh, E. C.; Boutareaud, S.; Song, S. R.; Tsai, C. H. *Geochem. Geophys. Geosyst.* **2009**, *10*, 1.
- (7) Matsuda, T.; Omura, K.; Ikeda, R.; Arai, T.; Kobayashi, K.; Shimada, K.; Tanaka, H.; Tomita, T.; Hirano, S. *Tectonophysics* **2004**, *378*, 143.
- (8) Saffer, D. M.; Frye, K.; Marone, C.; Mair, K. *Geophys. Res. Lett.* **2001**, *28*, 2297.
- (9) Vrolijk, P. *Geology* **1990**, *18*, 703–707.
- (10) Nagelschmidt, G. Z. *Kristallogr.* **1936**, *93*, 481.
- (11) Bradley, W. F.; Grim, R. E.; Clark, G. F. Z. *Kristallogr.* **1937**, *97*, 216.
- (12) Mooney, R. W.; Keenan, A. G.; Wood, L. A. *J. Am. Chem. Soc.* **1952**, *74*, 1371.
- (13) Norrish, K. *Faraday Discuss.* **1954**, *18*, 120.
- (14) Walker, G. F. *Clays Clay Miner.* **1956**, *4*, 101.
- (15) Méring, J.; Glaeser, R. *Bull. Soc. Fr. Mineral. Cristallogr.* **1954**, *77*, 519.
- (16) Glaeser, R.; Méring, J. C.R. *Acad. Sci.* **1968**, *267*, 463.
- (17) Glaeser, R.; Méring, J. *Clay Miner. Bull.* **1954**, *2*, 188.
- (18) Sato, T.; Murakami, T.; Watanabe, T. *Clays Clay Miner.* **1996**, *44*, 460.
- (19) Sato, T.; Watanabe, T.; Otsuka, R. *Clays Clay Miner.* **1992**, *40*, 103.
- (20) Ferrage, E.; Lanson, B.; Sakharov, B. A.; Drits, V. A. *Am. Mineral.* **2005**, *90*, 1358.
- (21) Bérend, I.; Cases, J. M.; François, M.; Uriot, J. P.; Michot, L. J.; Masion, A.; Thomas, F. *Clays Clay Miner.* **1995**, *43*, 324.
- (22) Cases, J. M.; Bérend, I.; Besson, G.; François, M.; Uriot, J. P.; Thomas, F.; Poirier, J. P. *Langmuir* **1992**, *8*, 2730.
- (23) Cases, J. M.; Bérend, I.; François, M.; Uriot, J. P.; Michot, L. J.; Thomas, F. *Clays Clay Miner.* **1997**, *45*, 8.
- (24) Cuadros, J. *Am. J. Sci.* **1997**, *297*, 829.
- (25) Ferrage, E.; Kirk, C. A.; Cressey, G.; Cuadros, J. *Am. Mineral.* **2007**, *92*, 994.
- (26) Ferrage, E.; Lanson, B.; Sakharov, B. A.; Geoffroy, N.; Jacquot, E.; Drits, V. A. *Am. Mineral.* **2007**, *92*, 1731.
- (27) Ferrage, E.; Lanson, B.; Malikova, N.; Plançon, A.; Sakharov, B. A.; Drits, V. A. *Chem. Mater.* **2005**, *17*, 3499.
- (28) Moore, D. M.; Reynolds, R. C., Jr. *X-ray Diffraction and the Identification and Analysis of Clay Minerals*; Oxford University Press: New York, 1997.
- (29) Alcover, J. F.; Gatineau, L. *Clay Miner.* **1980**, *15*, 239.
- (30) Alcover, J. F.; Gatineau, L. *Clay Miner.* **1980**, *15*, 25.
- (31) Mathieson, A. M. *Am. Mineral.* **1958**, *43*, 216.
- (32) Mathieson, A. M.; Walker, G. F. *Am. Mineral.* **1954**, *39*, 231.
- (33) Calle, C. d. l.; Pezerat, H.; Gasperin, M. *J. Phys. (Paris)* **1977**, *38*, 128 C7.
- (34) Calle, C. d. l.; Suquet, H.; Dubernat, J.; Pezerat, H. *Clay Miner.* **1978**, *13*, 275.
- (35) Slade, P. G.; Stone, P. A.; Radoslovitch, E. W. *Clays Clay Miner.* **1985**, *33*, 51.
- (36) Chang, F. R. C.; Skipper, N. T.; Sposito, G. *Langmuir* **1998**, *14*, 1201.
- (37) Delville, A. *J. Phys. Chem.* **1993**, *97*, 9703.
- (38) Chang, F. R. C.; Skipper, N. T.; Sposito, G. *Langmuir* **1995**, *11*, 2734.
- (39) Chang, F. R. C.; Skipper, N. T.; Sposito, G. *Langmuir* **1997**, *13*, 2074.
- (40) Rinnert, E.; Carteret, C.; Humbert, B.; Fragneto-Cusani, G.; Ramsay, J. D. F.; Delville, A.; Robert, J. L.; Bihannic, I.; Pelletier, M.; Michot, L. J. *J. Phys. Chem. B* **2005**, *109*, 23745.
- (41) Park, S. H.; Sposito, G. *J. Phys. Chem. B* **2000**, *104*, 4642.
- (42) Marry, V.; Turq, P. *J. Phys. Chem. B* **2003**, *107*, 1832.
- (43) Greathouse, J. A.; Storm, E. W. *Mol. Simul.* **2002**, *28*, 633.
- (44) Boek, E. S.; Coveney, P. V.; Skipper, N. T. *J. Am. Chem. Soc.* **1995**, *117*, 12608.
- (45) Calle, C. d. l.; Plaçon, A.; Pons, C. H.; Dubernat, J.; Suquet, H.; Pezerat, H. *Clay Miner.* **1984**, *19*, 563.
- (46) Tellera, M. I.; Slade, P. G.; Radoslovitch, E. W. *Clays Clay Miner.* **1977**, *25*, 119.
- (47) Rausell-Colom, J. A.; Fernandez, M.; Serratos, J. M.; Alcover, J. F.; Gatineau, L. *Clay Miner.* **1980**, *15*, 37.
- (48) Greathouse, J.; Sposito, G. *J. Phys. Chem. B* **1998**, *102*, 2406.
- (49) Skipper, N. T.; Chang, F. R. C.; Sposito, G. *Clays Clay Miner.* **1995**, *43*, 285.
- (50) Skipper, N. T.; Sposito, G.; Chang, F. R. C. *Clays Clay Miner.* **1995**, *43*, 294.
- (51) Marry, V.; Turq, P.; Cartiailler, T.; Levesque, D. *J. Chem. Phys.* **2002**, *117*, 3454.
- (52) Michot, L. J.; Bihannic, I.; Pelletier, M.; Rinnert, E.; Robert, J.-L. *Am. Mineral.* **2005**, *90*, 166.
- (53) Sakharov, B. A.; Naumov, A. S.; Drits, V. A. *Dokl. Akad. Nauk* **1982**, *265*, 871.
- (54) Sakharov, B. A.; Naumov, A. S.; Drits, V. A. *Dokl. Akad. Nauk* **1982**, *265*, 339.
- (55) Sakharov, B. A.; Drits, V. A. *Clays Clay Miner.* **1973**, *21*, 15.
- (56) Drits, V. A.; Sakharov, B. A.; Lindgreen, H.; Salyn, A. *Clay Miner.* **1997a**, *32*, 351.
- (57) Guinier, A. *Théorie et technique de la radiocristallographie*; Dunod: Paris, France, 1964.

(58) Drits, V. A.; Tchoubar, C. *X-ray diffraction by disordered lamellar structures: Theory and applications to microdivided silicates and carbons*; Springer-Verlag: Berlin, Germany, 1990.

(59) Ferrage, E.; Tournassat, C.; Rinnert, E.; Lanson, B. *Geochim. Cosmochim. Acta* **2005**, *69*, 2797.

(60) Howard, S. A.; Preston, K. D. In *Modern Powder Diffraction*; Bish, D. L., Post, J. E., Eds.; Mineralogical Society of America: Washington, D.C., 1989; Vol. 20, pp 217.

(61) Plançon, A. *Am. Mineral.* **2002**, *87*, 1672.

(62) Tambach, T. J.; Bolhuis, P. G.; Hensen, E. J. M.; Smit, B. *Langmuir* **2006**, *22*, 1223.

(63) Tambach, T. J.; Hensen, E. J. M.; Smit, B. *J. Phys. Chem. B* **2004**, *108*, 7586.

(64) Ferrage, E.; Kirk, C. A.; Cressey, G.; Cuadros, J. *Am. Mineral.* **2007**, *92*, 1007.

(65) Moore, D. M.; Hower, J. *Clays Clay Miner.* **1986**, *34*, 379.

(66) Besson, G.; Misfud, A.; Tchoubar, C.; Méring, J. *Clays Clay Miner.* **1974**, *22*, 379.

(67) Besson, G.; Glaeser, R.; Tchoubar, C. *Clay Miner.* **1983**, *18*, 11.

(68) Rinnert, E., Ph.D. Thesis, Université Nancy, 2004.

(69) Calle, C. d. I.; Suquet, H.; Pezerat, H. *Clay Miner.* **1985**, *20*, 221.

(70) Pezerat, H. *C.R. Acad. Sci.* **1967**, *265*, 529.

(71) Pezerat, H.; Méring, J. *Bull. Groupe Fr. Argiles* **1958**, *10*, 25.

(72) Michot, L. J.; Villiéras, F. *Clay Miner.* **2002**, *37*, 39.

JP909860P